

Label-free single-cell microfluidics reveals antibiotic transport kinetics in Gram-negative bacteria

Authors: Jehangir Cama^{1,2*†}, Margaritis Voliotis^{1†}, Jeremy Metz¹, Ashley Smith¹, Jari Ianucci¹, Ulrich F. Keyser², Krasimira Tsaneva-Atanasova¹ and Stefano Pagliara^{1*}.

Affiliations:

¹Living Systems Institute, University of Exeter, Exeter EX4 4QD, United Kingdom.

²Cavendish Laboratory, Department of Physics, University of Cambridge, JJ Thomson Avenue, Cambridge CB3 0HE, United Kingdom.

*Correspondence to: j.cama@exeter.ac.uk, S.Pagliara@exeter.ac.uk

†J. Cama and M. Voliotis contributed equally to this work.

Abstract: The double-membrane cell envelope of Gram-negative bacteria is a formidable barrier to the cellular entry of antibiotics. Therefore, quantifying antibiotic accumulation in these bacteria is crucial for Gram-negative drug development. However, there is a dearth of techniques capable of studying the kinetics of drug accumulation in single bacteria while also controlling the surrounding microenvironment. By combining microfluidics and time-lapse auto-fluorescence microscopy, we quantified ofloxacin uptake label-free in hundreds of individual *Escherichia coli* bacteria revealing homogeneous kinetics of drug accumulation within clonal populations. By manipulating the microenvironment, we showed that ofloxacin accumulation is higher in growing versus non-growing cells. We investigated mutants lacking major transport proteins to inform a new Bayesian hierarchical model that quantifies the kinetics of ofloxacin uptake in individual bacteria. Importantly, our combined experimental-theoretical approach predicts drug accumulation in subcellular compartments, which is essential for the rational design of new Gram-negative antibiotics.

Introduction:

Antibiotic failure in the treatment of microbial infections is fast being recognized as the pre-eminent public health threat facing the World today, with projections estimating that drug resistant infections will cause 10 million deaths *annually* by 2050 (1). Gram-negative bacterial infections are of particular concern; their double-membrane cell envelopes, with asymmetric outer membranes containing lipopolysaccharide (LPS) molecules, create a formidable permeability barrier to the cellular entry of both hydrophilic and hydrophobic molecules (2,3). Antibiotic permeation across the outer membrane is therefore dependent on the drug's ability to utilize protein pores (or *porins*) (4), typically used for nutrient uptake, to circumvent this barrier. These porins show a preference for hydrophilic, charged compounds; however, to reach their (typically) cytoplasmic targets, the same molecules have to also cross the inner membrane phospholipid bilayer, which acts as a selectivity barrier *against* polar, charged molecules (2,3). Additionally,

Gram-negative bacteria harbor active efflux mechanisms, which pump toxic compounds out of the cell (5). Successful drugs must minimize their propensity for recognition and removal by these efflux pumps, in addition to displaying specific physicochemical properties to permeate both through the outer membrane porins and inner membrane phospholipids (2). This complex membrane transport landscape has led to a major void in Gram-negative antibiotic discovery, with no new classes of broad-spectrum drugs being introduced in the past 50 years (6). Inevitably, this has led to the emergence of pan-drug resistant (PDR) Gram-negative infections, for which we currently have no viable treatment (7).

There is thus a critical need to understand the physical pathways and molecular mechanisms associated with antibiotic permeation across the Gram-negative cell envelope. These mechanisms are further complicated by the fact that the expression and activity of porins and efflux pumps vary i) with the microenvironment conditions (8) and ii) within an isogenic population exposed to the same environmental landscape (9). Many existing techniques suffer from the requirement of complex washing steps (3,10), with cells only studied after resuspension in contrived nutrient environments (11,12); the washes also increase the chance of cell lysis and efflux or diffusion of the analyte from the cells, besides affecting cellular physiology. Furthermore, the most commonly used techniques are population level assays which cannot investigate heterogeneity in uptake at the single-cell or at the subcellular level. Finally, most of the available techniques only provide a static picture of drug accumulation rather than the full kinetics of drug uptake. We require techniques that can quantify antibiotic accumulation in individual bacteria, which must be capable of studying cells after exposure to different nutrient conditions or in different metabolic states. Ideally, these should also be simple to implement, the standardization of such techniques being critical to ensure their uptake in pharmaceutical companies and in clinical settings.

We address these challenges by repurposing the microfluidic “mother-machine” (13) for quantitative measurements of drug accumulation and kinetics in up to hundreds of individual bacteria per experiment. We investigated three *Escherichia coli* strains from the Keio collection, encompassing the parental strain (PS) BW25113, a porin knockout ($\Delta ompF$) and an efflux protein knockout ($\Delta tolC$) strain (Figure 1A). A small aliquot of bacterial culture was seeded into the device (Figure 1B) and dosed with the fluoroquinolone antibiotic ofloxacin (12.5 $\mu\text{g/ml}$) either in a non-growing or a growing state. Ofloxacin delivery and its accumulation in the bacteria was tracked using *time-lapse near-ultraviolet auto-fluorescence* microscopy (Figure 1C-D). We then modelled (Figure 1A) the uptake process (14) across the three strains to estimate the kinetic parameters associated with early stage ofloxacin uptake (up to $t = 400$ s). We used Bayesian inference to investigate how specific model parameters varied between individual cells in the different strains. Finally, we used the parameters obtained from the modelling to predict the kinetics of drug accumulation in the various subcellular compartments of the cells across the different strains.

Results:

Quantifying drug dosage:

Our experimental approach, using syringe pumps to control drug delivery and auto-fluorescence for drug detection (Methods), enables us to precisely quantify the arrival of the drug in the vicinity of the cells under investigation. Representative images of the main, drug delivery channel and the side, cell-hosting channels before and after drug dosage are shown in Figure 1C. Example drug dosage profiles are reported in Figure 2 (dashed black lines) and in the ESI (dashed black lines in

Figures S1A,C and S6). Since the drug dosage concentration is the same across all experiments, this measurement allows us to correct for any drug fluorescence intensity variation across all the different experiments (Methods). We measure the background at $t = 0$, and observe that the drug arrives in the field of view typically around 100 s after the start of the experiment, reaching its final concentration around 200 s (Figure 2A-D). We use the final, steady-state value of the drug dose fluorescence (at $t = 400$ s) to map drug fluorescence to drug concentration (see Methods). Importantly, since we measure the drug dosage profile across different experiments, we use this information as an input to the model, which allows us to account for any differences between the dose profiles across the different experiments.

Quantifying cellular auto-fluorescence:

For each strain/condition, we performed control experiments to measure the auto-fluorescence profiles of individual bacteria in the absence of the drug (see Methods). A representative comparison between cellular drug fluorescence and auto-fluorescence profiles is reported in Figure S1, corresponding to either the presence (Figure S1A,C) or absence (Figure S1B,D) of the drug. We observe that the cellular control auto-fluorescence profiles are flat across the timescales of the experiment; thus cellular auto-fluorescence has a negligible effect on the drug uptake profiles. Similar cellular auto-fluorescence profiles were observed across all the control experiments performed (number of biological repeats: 2 (PS growing), 3 ($\Delta ompF$ growing), 2 ($\Delta tolC$ growing), 3 (PS non-growing) and 3 ($\Delta tolC$ non-growing) – data not shown).

Ofloxacin uptake is homogeneous across a clonal population:

A major advantage of single-cell approaches is their ability to quantify heterogeneity (or the lack thereof) in the cellular response to treatment within the individual cells in a population. In order to estimate heterogeneity in drug uptake across the bacteria, we first estimated the variation in cellular fluorescence in the absence of the drug and found a mean coefficient of variation (CV) of approximately 10% (see Methods). We found a similar CV when quantifying the heterogeneity in the cellular fluorescence corresponding to drug uptake. As seen in Figure S6, such variation is representative across the biological repeats. We thus conclude that ofloxacin uptake is homogeneous across the clonal populations that we studied, which is remarkable considering the recent reports on cellular heterogeneity within microbial populations (9).

Cellular drug uptake profiles:

Figure 2A-D report bacterial drug uptake profiles (red lines) from representative experiments studying growing PS (2A), non-growing PS (2B), growing $\Delta ompF$ (2C) and growing $\Delta tolC$ (2D) *E. coli*. The drug uptake profiles for $\Delta tolC$ (non-growing) *E. coli* and all the biological repeats performed are reported in Figure S6.

We observe an increase in cellular drug fluorescence within seconds after the arrival of the drug in the vicinity of the cells. Please note that previous population-level studies have shown biphasic ofloxacin uptake in *E. coli* over longer timescales of up to an hour (15), but here we focus our attention on the initial stages of drug uptake, studying the immediate cellular response to drug dosage ($t \leq 400$ s) at the single-cell level.

1. Growing bacteria accumulate more ofloxacin than non-growing bacteria:

Comparing growing versus non-growing PS cells (Figure 2A-B) immediately reveals that growing cells accumulate more ofloxacin than non-growing cells. To quantify this difference, we compared the distributions of cellular fluorescence (normalized to the value of drug fluorescence) at $t = 400$ s across all biological repeats in Figure 3 (see Methods). In all datasets, growing PS cells show an approximately 3-fold higher fluorescence than non-growing cells (**growing**: norm. fluor. = 0.34 ± 0.11 , $N = 317$, mean \pm s.d.; **non-growing**: norm. fluor. = 0.10 ± 0.03 , mean \pm s.d., $N = 405$; $p < 10^{-10}$). A similar result was obtained when comparing growing and non-growing cells in the $\Delta tolC$ mutant strain (**growing**: norm. fluor. = 0.31 ± 0.08 , $N = 211$, mean \pm s.d.; **non-growing**: norm. fluor. = 0.12 ± 0.06 , mean \pm s.d., $N = 193$; $p < 10^{-10}$).

2. Knocking out *ompF* lowers ofloxacin accumulation compared to the PS:

From Figure 2A and 2C, we also observe that the growing $\Delta ompF$ mutant strain accumulates lower amounts of ofloxacin than the PS over the timescales investigated. This is quantified in Figure 3 ($\Delta ompF$: norm. fluor. = 0.20 ± 0.11 , mean \pm s.d., $N = 250$; **PS**: norm. fluor. = 0.34 ± 0.11 , $N = 317$, mean \pm s.d.; $p < 10^{-10}$); knocking out the OmpF porin thus lowers the ability of ofloxacin to permeate into the cell compared to the parental strain. Our result agrees with previous reports that show that OmpF facilitates fluoroquinolone transport across Gram-negative outer membranes. (4,16).

3. Knocking out *tolC* does not increase ofloxacin accumulation compared to the PS:

Interestingly, we were unable to detect an increase in ofloxacin accumulation in growing $\Delta tolC$ mutant cells compared to the PS at the 400 s time-point (Figure 3). In fact, as reported above, we measured a small *decrease* in the drug fluorescence in growing $\Delta tolC$ cells compared to the growing PS cells ($\Delta tolC$: norm. fluor. = 0.31 ± 0.08 , $N = 211$, mean \pm s.d.; **PS**: norm. fluor. = 0.34 ± 0.11 , $N = 317$, mean \pm s.d.; $p = 2.7 \times 10^{-4}$). This counter-intuitive finding is addressed in detail in the Discussion.

Theoretical model of drug transport across the Gram-negative cell envelope:

The quantitative comparisons above provide a *static* picture regarding the impact of porins, pumps and growth stages on ofloxacin accumulation in Gram-negative bacteria at the *whole-cell level*. However, the most desirable information concerns the *kinetics* of drug accumulation in the different *subcellular compartments*. It is crucial to understand how much of a drug actually reaches its target which, in the case of ofloxacin, lies in the cytoplasm (17). We rationalize our experimental drug uptake data via mathematical modelling and show that we can extract the essential parameters governing drug uptake kinetics. In particular, we model drug uptake in the different compartments of a Gram-negative bacterium (Figure 1A) using the following set of ordinary differential equations (ODEs):

$$V_M \frac{dD_M}{dt} = k_1 D_O (M_0 - D_M) + k_1 D_P (M_0 - D_M) - 2k_2 D_M \quad (i)$$

$$V_P \frac{dD_P}{dt} = k_2 D_M - k_1 D_P (M_0 - D_M) - k_3 D_P + k_3 D_C + k_4 D_O - k_4 D_P - v \frac{D_P}{K_m + D_P} \quad (\text{ii})$$

$$V_C \frac{dD_C}{dt} = (k_3 D_P - k_3 D_C) \quad (\text{iii})$$

where D_O , D_M , D_P and D_C denote the drug concentrations in the external environment, the outer membrane, the periplasm and the cytoplasm, respectively. Importantly, we used the measured drug dosage traces for estimating D_O for every experiment, which allows us to control for any variations in the drug dosage profiles across different experiments (Figure S6). We model porin-mediated drug transport through the outer membrane as a two-step reversible process: drug molecules bind to porins with rate constant k_1 from either side of the outer membrane and unbind to either side at rate k_2 . M_0 denotes the concentration of functional porins in the outer membrane. As a first approximation, we assume that diffusion through the LPS-lipid bilayer is negligible ($k_4 \sim 0$) in comparison to porin-mediated transport (3). Furthermore, we postulate that ofloxacin molecules, like other fluoroquinolones (18,19), diffuse across the inner membrane lipid bilayer (rate constant k_3) and that the efflux of drug molecules from the periplasm to the external medium follows Michaelis-Menten kinetics with maximal rate v and Michaelis constant K_m (14). Finally, parameters V_M , V_P and V_C denote the volumes of the outer membrane, periplasm and cytoplasm, respectively (Table S2). The parameter k_3 was calculated on the basis of passive diffusion measurements of ofloxacin permeability across lipid vesicle bilayers (Figure S3); importantly, the remaining parameters (k_1 , k_2 , M_0 , K_m , v) were inferred from the experimental data obtained with the PS, $\Delta ompF$ and $\Delta tolC$ *E. coli* strains (Figure S6). The total drug concentration is calculated as:

$$D_T = \frac{D_M * V_M + D_P * V_P + D_C * V_C}{V_M + V_P + V_C} \quad (\text{iv})$$

To model drug uptake in the $\Delta ompF$ strain, we used the set of equations presented above, additionally assuming a possible decrease in the number of porins relative to the PS, i.e., $M_{0,\Delta ompF} \leq M_0$. Similarly, for the case of the $\Delta tolC$ strain, we assumed that the *maximal* efflux rate may decrease relative to the PS, i.e., $v_{\Delta tolC} \leq v$.

We obtained maximum likelihood estimates (MLEs) of the free model parameters (Table S2) using population-averaged (i.e., all cells in an experiment) drug uptake profiles (see Methods). Since the data used for fitting the model was normalized based on the fluorescence of the drug dose (see Methods), parameters k_1 , M_0 , K_m , v are proportional to a constant factor related to the concentration of the drug dose (Table S2). We denote the scaled version of these parameters using the prime symbol (''). We used a Bayesian hierarchical version of the model where we assumed parameters M_0 and v vary according to a log-normal distribution across the bacterial population within an experiment. In fact, a previous study predicted log-normal distributions for protein abundances in *E. coli* cells, at least during steady state growth (20). Similar log-normal distributions were also observed when studying reporter genes located both on the genome and on plasmids, suggesting that log-normal distributions are ubiquitous in such cellular systems (20). Parameter priors in the Bayesian hierarchical model were informed using the MLEs obtained from the population-averaged data (Methods). Posterior estimates of the population parameters were then obtained from the single-cell data after running a Gibbs sampler for 2000 iterations. The results of the parameter distributions for growing bacteria from the three investigated strains are

presented in Figure 4A-B; the different biological repeats are signified by solid, dotted and dashed lines (PS, red; $\Delta ompF$, blue; $\Delta tolC$, green). We found similar values across the different biological replicates for the PS cells, whereas the knockout mutants showed greater variability both between replicates and within individual experiments, as observed in Figure 4A-B. The parameter estimations also reveal lower porin concentrations and maximal efflux rates in the mutants compared to the PS, rationalizing the lower drug accumulation observed in these strains.

We note that, as discussed above, the non-growing cells showed a significantly lower increase in intracellular drug fluorescence when compared to growing cells (Figures 2 and 3). When we fit this data to our model, we obtained poor fits due to the flatness of the uptake profiles; these profiles do not provide enough information for the model to predict kinetic parameters. We also observed a similar uptake profile in one of the growing $\Delta ompF$ experiments (Figure S6B, middle panel) and therefore this dataset was not included in the modelling results in Figures 4 and 5.

Model predictions for ofloxacin accumulation in subcellular compartments:

Once the model parameters were inferred from all the individual experiments (using the corresponding drug dosage profiles for each experiment), we used these parameters in the model to estimate the drug accumulation in the various subcellular compartments for cells belonging to the three strains (Figure 4C). In this estimation for Figure 4C, we used an average experimental drug dosage profile (dashed black line, top panel, Figure 4C) as the input for D_0 . The overlap (or lack thereof) between the [20,80] posterior predictive intervals (shaded regions in Figure 4C) allows us to predict the probability of PS cells having a higher/lower ofloxacin concentration than each of the mutants, at the subcellular level. The pairwise comparisons (at $t = 400$ s) for the different strains/compartments are presented in Table S4.

The model predicts that the drug saturates all the binding sites in the outer membrane within approximately 150 s in all three strains. The PS strain has the highest outer membrane drug concentration, with the $\Delta ompF$ mutant having a 3-fold lower concentration, which corresponds to the fewer binding sites available in the mutant (Figure 4A). At the end of the experiment, the probability that the PS strain has a higher drug concentration than the $\Delta ompF$ mutant in the outer membrane is 0.963; between the PS and the $\Delta tolC$ mutant, the probability that the PS has more drug in the outer membrane is 0.831 (Table S4).

The periplasm and cytoplasm always show a similar drug concentration (within the same strain) – this is a feature of the model which predicts, based on the lipid permeability of ofloxacin, that the drug rapidly (within seconds) equilibrates between these two compartments. We do however observe a lag time of approximately 100 s between drug accumulation in the outer membrane versus drug uptake in the periplasm and cytoplasm. In these two compartments, the difference between the PS and the mutant strains is less obvious. The model predicts that, at the end of the experiment, the PS strain has a probability of 0.658 of having a higher drug concentration in the cytoplasm than the $\Delta ompF$ mutant (Table S4). Comparing the PS and the $\Delta tolC$ mutant, the corresponding probability is 0.46.

Discussion:

Drug uptake in Gram-negative bacteria is an extremely complex biophysical phenomenon because of the different physicochemical pathways and combination of active and passive transport processes involved. However, it is essential to understand the roles of these pathways in a quantitative manner to rationally design drugs that can accumulate in the vicinity of their targets, which will be crucial to overcome the void in Gram-negative drug discovery.

We have developed a novel combination of experiment and theoretical modelling to tackle the challenge of quantifying antibiotic uptake in single Gram-negative bacteria. Unlike the majority of techniques, which involve complex washing steps after drug delivery, or are limited to certain specific media conditions (3,10), our microfluidic platform facilitates the study of drug uptake in different microenvironments and cellular metabolic states. We quantify drug dosage in every experiment, which allows us to correct for any variations in fluorescence intensities/flow conditions between experiments. Since we use microfluidics, we quantify drug uptake from the moment the drug arrives in the vicinity of the cells, facilitating the real-time measurement of the transport process.

It is worth noting that we can measure over a hundred cells in an experiment; by reducing the time resolution it is also possible to correspondingly increase the number of cells measured, since typically thousands of cells are confined in the microfluidic device. This ability will be used in future studies, especially for drugs whose uptake timescales are longer than fluoroquinolones.

Further, unlike previous studies using deep UV illumination to study antibiotic uptake in single cells (11,21), since our excitation wavelength is 365 nm, we can work with standard optics and light sources, rather than needing quartz objectives and cover slips, and deep UV light sources which may not be easily accessible.

Our experimental data shows clearly that within the timescales investigated, ofloxacin accumulates to a greater degree in growing versus non-growing bacteria (Figures 2 and 3). It is likely that this reduction in ofloxacin accumulation contributes to the significant increase in cell survival to this drug that was previously observed as the cells enter stationary phase compared with early exponential phase cultures (22,23). Our results also correlate with population level transcriptomic data, which showed that the genes encoding the major *E. coli* porins OmpF and LamB, through which fluoroquinolones diffuse, were upregulated in exponentially growing compared to stationary phase *E. coli* cells (22).

Knocking out the *ompF* gene led to a decrease in drug accumulation compared to the parental strain, in line with previous results (4), confirming that fluoroquinolones utilize porins to enter *E. coli* cells. However, as described in the Results, we did not measure any increase in drug accumulation in the $\Delta tolC$ strain. These mutants lack the TolC outer membrane efflux protein, which forms an important part of multi-drug efflux systems such as AcrAB-TolC that eject antibiotics and other toxins from *E. coli* cells (24), and naively one would have expected that losing TolC negatively affects the ability of the cell to efflux the antibiotic, thus increasing its intracellular accumulation. It has also been reported that the inactivation of *tolC* increases the susceptibility of bacteria to a range of antibacterial agents, ostensibly due to the inactivation of the corresponding efflux systems (24). However, although the overproduction of the AcrAB-TolC efflux system has been implicated in the antibiotic resistance of clinical isolates of *E. coli* species, there was no significant correlation between the overexpression of the *acrAB* and *tolC* genes (24,25). Specifically, with regards to fluoroquinolone antibiotics, it was reported that average *tolC*

expression levels in fluoroquinolone-susceptible and fluoroquinolone-resistant clinical isolates of *E. coli* were not statistically different (24,25). Zgurskaya and co-workers therefore concluded that TolC quantities alone do not limit the drug efflux capabilities of *E. coli* (24). Our data further corroborate this hypothesis.

The use of mathematical modelling and Bayesian inference to rationalize our data enabled us to maximize the information embedded in our time-lapse single-cell measurements, by estimating the *kinetics* of the uptake process. We extracted kinetic parameters corresponding to the single-cell drug uptake profiles and quantified changes in these parameters in the different strains (Figure 4A-B). Importantly, this approach allowed us to use these parameters in our model to predict drug accumulation in the different subcellular compartments, which is a major aim for the entire research community working on this problem. Future work will involve studying drug accumulation after modulation of other transport pathways in the Gram-negative double membrane to estimate their relative contributions to drug uptake at the subcellular level.

Our single-cell platform allows us to quantify heterogeneity in the cellular response to antibiotic treatment (26). However, as detailed in the Results section, quantitative estimates of systematic and biological variation revealed no detectable heterogeneity in ofloxacin uptake in our experiments. Considering the large variations in gene and protein expression reported in bacterial cells and the corresponding phenotypic heterogeneity (9,27), it is striking that ofloxacin uptake appears to be uniform across cells within each of our experiments. This may be the result of using a high dosage concentration of ofloxacin (100×MIC, 12.5 µg/ml); as described by the model results, the outer membrane of all the strains saturates within 150 s, and hence small differences in the expression of different transport pathways might be missed. Our high dosage concentration may also explain why, although there is a significant reduction in drug accumulation in the outer membrane of the $\Delta ompF$ mutant strain compared to the PS, the model predicts that median cytoplasmic concentrations of the drug in the PS are only approximately 20% higher than in the $\Delta ompF$ mutant (Figure 4C, Table S4).

Conclusions:

We have developed a novel experimental and theoretical approach to study antibiotic accumulation label-free in individual Gram-negative bacteria in well-controlled microenvironments. Our experiments enabled us to quantify the role of the nutrient microenvironment and metabolic state of the cells in drug uptake at the single-cell level. Combining our data with mathematical modelling and Bayesian inference enabled us to predict the kinetic parameters underlying ofloxacin accumulation in the different subcellular compartments of *E. coli* cells. This has previously proved extremely challenging primarily due to the small size of typical bacterial cells and the need for complicated washing steps before measuring drug uptake (3,10), which may bias the results. We used the parameters extracted from fitting the model to our experimental data to predict drug accumulation in the outer membrane, the periplasm and the cytoplasm in parental, $\Delta ompF$ and $\Delta tolC$ *E. coli*.

Our approach offers possibilities for scaling up the number of drugs that can be tested on the same chip, via parallelization of the cell trapping chambers. We also require small volumes of concentrated cultures for seeding the chip (<10 µl), which may facilitate its use in clinical settings. The assay also has the advantage of needing only micrograms of chemicals for testing, which is

important when evaluating novel, candidate drugs that are typically expensive to manufacture. Our readout is based on fluorescence, and can be used to test the permeation properties of newly developed fluorescent antibiotic probes (28), providing information about Gram-negative drug permeability for a range of different antibiotic classes. The experimental setup is relatively simple to implement on standard epi-fluorescence microscopes and will provide researchers with a new, transferrable platform with which to study this vitally important permeation process in a range of Gram-negative species.

Materials and Methods:

Chemicals:

Chemicals were purchased from Sigma-Aldrich unless otherwise stated. Ofloxacin stock solutions were prepared at a concentration of 10 mg/ml in 1 M NaOH. For the ofloxacin uptake experiments, the stock was diluted to a concentration of 12.5 µg/ml (100×MIC) in PBS. The minimal media used in the experiments was prepared in sterile water and contained 1×M9 salts, 2 mM MgSO₄, 0.1 mM CaCl₂ and 1 mM thiamine hydrochloride. The LB medium used for cell culture was the Melford high salt version containing 10 g/L casein digest peptone, 5 g/L yeast extract and 10 g/L NaCl; LB Agar plates were prepared with 15 g/L agar. Glucose stock solutions were prepared at a concentration of 0.5 M in sterile water and diluted to 1 g/L in minimal media for use in the experiments. Stock solutions of bovine serum albumin (BSA) were prepared at a concentration of 50 mg/ml in sterile water. A stock solution of propidium iodide (PI) was purchased from Thermo Fisher Scientific, and diluted 1:1000 in PBS for use in the experiments.

Bacterial cell culture:

All the *E. coli* strains used were BW25113 strains purchased from the Keio collection. The mutant strains contained kanamycin resistance cassettes in place of the deleted chromosomal gene. The strains were stored at -80 °C in a 1:1 ratio of overnight culture and 50% glycerol solution. 200 ml cultures were grown in LB (with 25 µg/ml kanamycin) at 37 °C overnight (with shaking at 200 rpm). Streak plates were prepared on LB agar (containing 25 µg/ml kanamycin), stored at 4 °C and used for a maximum of one week.

Microfluidic chip fabrication:

The complete protocol for the fabrication of the “mother-machine” microfluidic devices was reported previously (26). The epoxy mold used was constructed from replicas of devices kindly provided by the Jun lab (29). The final devices used were created by pouring polydimethylsiloxane (PDMS, Dow Corning, 9:1 base : curing agent) on to the epoxy mold; the PDMS was baked at 70 °C for 2 h in an oven. The PDMS chips were cut out and fluidic inlet/outlet columns punched using a 1.5 mm biopsy punch (Milten). The PDMS chips were bonded to a type 1 coverslip using an air plasma treatment (10 s exposure at 30 W plasma power, Plasma etcher, Diener electronic GmbH, Germany) and left at 70 °C for 5 min to improve the adhesion. The chips were then filled with a 50 mg/ml solution of bovine serum albumin (BSA, in milliQ water) and incubated at 37 °C for 1

h. The BSA treatment passivates the internal surfaces of the chip thus preventing cells from adhering to the microchannels during experiments.

An overnight culture of cells was resuspended in spent LB and concentrated to an OD of 50 (at 595 nm). The spent LB was prepared by centrifuging the overnight culture (10 min at 3000 g and 20 °C) – the supernatant was filtered twice through a 0.2 µm pore filter (Millipore). A 2 µl aliquot of this solution was injected into the microfluidic device and incubated at 37 °C for 20 min, enabling cells to enter the small side channels of the device. The filled device was then left overnight at room temperature before starting experiments.

Drug uptake assay:

Microfluidic flows were controlled using three parallel neMESYS syringe pumps (Cetoni GmbH, Germany) with glass syringes (ILS, Germany) of volumes 5 ml, 250 µl and 100 µl respectively. The syringes were interfaced with the microfluidic chips using FEP tubing (Upchurch Scientific 1520, I.D. = 0.03” and O.D. = 0.0625”). The syringes and the associated tubing were rinsed thoroughly with milliQ water and the appropriate experimental solutions before beginning the experiments, and with 70% ethanol after completion of the experiments.

All the experiments were performed on an Olympus IX73 epifluorescence microscope with an LED light source (wLS pE300, QImaging) using a 365 nm excitation wavelength LED. A standard DAPI filter set (Chroma ET series) modified with a ZET 365/20x excitation filter (Chroma) was used to better match the 365 nm excitation wavelength. An Olympus UPLSAPO 60×W (N.A 1.2) objective was used for all the experiments. We used a heating stage (Linkam Scientific THL60-16, UK) to maintain the cells at 37 °C throughout the experiments. All the ofloxacin experiments’ fluorescence intensity traces are presented in Figure S6 in the ESI.

For the experiments on growing cells, chips containing stationary phase *E. coli* were flushed with a continuous flow of fresh LB (100 µl/h) for 3 h. This was followed by a 10 min flush (at 300 µl/h) with minimal media containing 1 g/L glucose to wash away the LB. The glucose was added to the minimal media to prevent the cells from starving. Thereafter, ofloxacin (100×MIC, 12.5 µg/ml dissolved in PBS) was perfused through the chip at 100 µl/h, with images acquired at 5 s intervals using an Evolve 512 EMCCD camera (Photometrics) with 10 ms exposure times and an EM gain of 200 (bin 1, clearing mode – pre-exposure). The camera was controlled using µManager 1.4 (30). We chose to always dissolve the ofloxacin in PBS to ensure that the pH conditions remained uniform during drug exposure across all experiments and metabolic conditions; it is well known that pH regulates the charge state of fluoroquinolones, which affects their membrane permeabilities (18,19). The LED was triggered by the camera to ensure that the cells were only exposed to the excitation light during image acquisition. It must be noted that to reduce the background auto-fluorescence at 365 nm, prior to the ofloxacin flush the imaging area was bleached with the excitation light for 5 s. As detailed below, we performed controls (see Figure S2) with propidium iodide staining after UV and ofloxacin exposure to confirm that the UV light used did not compromise the cells’ membrane integrity.

For experiments on non-growing cells, the chips containing stationary phase *E. coli* were flushed for 10 min with PBS (300 µl/h) to wash away residual LB, the imaging area was bleached for 5 s

with the UV light (365 nm) and subsequently the ofloxacin was perfused through the chip, with the drug concentration and imaging settings exactly the same as for the growing cell experiments.

For both growing and non-growing cell experiments, we performed auto-fluorescence controls where instead of the ofloxacin, PBS was perfused through the chip (the rest of the protocols remained identical). A representative dataset is reported in Figure S1(B) in the ESI.

Image Analysis:

The image analysis was performed using a custom Python module (31). First, a specified range of frames of the dataset are loaded. Optionally, manually selected out-of-focus time-points are ignored. Cell detection is performed on a frame-by-frame basis as follows. First the frame is filtered using a Difference-of-Gaussian (DoG) scale-space filter (32) spanning a small range of scales, corresponding to the scale range of bacterial widths. The resulting scale-space volume is maximum-projected along the scale axis, and the automatic threshold detected using the Triangle method (33).

The centroids of the regions in the binary image resulting from applying this threshold are used to determine the axis of the side channels by using Principal Component Analysis. The axis of the side channels is then used to determine the upper and lower extents of the side-channel-region, which are then used to generate a side-channel-region mask, in addition to two candidate main-channel-region masks. The side-channel-region mask is then used to select bacterial regions from the binary image. The correct channel is identified from the two candidate regions by analysing the fluorescence for the region whose mean signal exhibits the most variation.

Cells are tracked frame-to-frame by matching positions such that nearest-matching bacteria are assigned only if the match is cross-validated in both forward and backward temporal directions (34). Bacterial trajectories are filtered to remove short trajectories (less than 10% of the full length).

The final trajectories are analysed as follows. First, a pre-determined dark-count (which is the average intensity of an image captured with the camera sensor covered) is subtracted from each bacterium's mean fluorescence, yielding the dark-count-corrected mean intensities. The corresponding dark-count-corrected PDMS background values for each bacterium are obtained by averaging the pixel intensity values of the PDMS to the immediate left and right of the individual bacterium and applying a similar dark-count correction. This bacterium-specific dark-count-corrected PDMS background is subtracted from the corresponding bacterium. Finally, the background subtracted bacterium's intensity at the starting time point is subtracted from all the values at later time points, yielding the background corrected bacterial fluorescence profiles over the course of the experiment (solid lines in Figures 2, S1 and S6).

For the drug dosage fluorescence, the initial intensity value of the dosage “main” channel (dark-count-corrected) is subtracted from all subsequent time points to initialise the drug fluorescence value to 0 (before drug arrival) – this also accounts for the subtraction of the background in the main channel. This reveals the drug dosage fluorescence profile over the course of the experiment (dashed lines in Figures 2, S1A,C and S6).

To account for any differences in absolute drug fluorescence between experiments, for the comparative analysis of drug uptake across the different experiments, all the background corrected cell and drug dosage fluorescence values in an experiment are normalised to the final value of the drug fluorescence in the main channel ($t = 400$ s) for that experiment. Note that this drug fluorescence value at $t = 400$ s is post-subtraction of the initial main channel background (measured before drug arrival) and thus always corresponds to the same concentration of ofloxacin ($100\times\text{MIC}$, $12.5\text{ }\mu\text{g/ml}$) across all experiments. These values are shown for a representative experiment in Figure 1D, and used for all comparative analysis (Figure 3) and modelling results in the paper. It is important to note that, since we are using this normalization in the model, we are assuming that the correspondence between drug fluorescence and concentration is the same in the main channel and in the vicinity of the cells. It is not possible to accurately resolve the drug fluorescence in the side channels in the immediate vicinity of each cell. The cells themselves are brighter than the surrounding channel and are hence easier to detect and track and, as specified above, we have established a protocol to subtract the scattering and fluorescence background for the cells.

Finally, since the cellular auto-fluorescence profiles were flat (Figure S1B,D), we did not need to correct for this effect when analysing the drug uptake experimental data; we simply subtracted the initial cellular fluorescence (at $t = 0$) from the cell fluorescence at all the time-points, as detailed above. We should also mention that the automated tracking works better for growing cells than for non-growing cells, which were smaller in size and therefore more difficult to detect. However, this does not significantly affect the average results, and the cell fluorescence values obtained through the automated code were similar to those obtained by manually selecting and measuring the cells in ImageJ; since we do not fit the model to the data for non-growing cells, we used the automated tracking results in all the figures in this manuscript.

Quantifying intra-experimental variability:

In order to estimate the variation in cellular fluorescence in the absence of the drug, we used the auto-fluorescence control experiment shown in Figure S1B to estimate the underlying biological and systematic variation in our experiments. These measurements report the *auto-fluorescence of the same cells* measured at different time points in the experiment. We quantified the coefficient of variation (CV) of the cell auto-fluorescence intensities (over the timescales of the experiment) of the 103 individual cells shown in Figure S1B. The *mean CV* across *all* the cells was $10 \pm 3\%$ ($N = 103$, mean \pm s.d.). This gives a quantitative estimate of the *measurement (systematic and underlying biological) heterogeneity for individual cells* within a single experiment.

We compare this variability in cellular auto-fluorescence with the apparent heterogeneity in drug uptake in the cells in Figure S1A. To estimate this value, we measured the intensity of the cells at the end of the drug uptake experiment ($t = 400$ s). The *heterogeneity in the cellular fluorescence corresponding to drug uptake* (in the knowledge that this includes the systematic and underlying biological variation mentioned above) is extracted by measuring the CV of the fluorescence across all the cells at this time-point. *Unlike* the CV measurement of the control which was for *individual cells* across *all* time-points, to estimate drug uptake heterogeneity amongst the 126 different cells, we measured the CV in the fluorescence of *all the cells* at the *final* time-point. This analysis yields a CV of 9.7%.

Model simulations:

All model simulations were run in Matlab (R2018b) using the in-built explicit Runge-Kutta (4, 5) solver (function ode45; default settings). The codes are available upon reasonable request.

Parameter estimation:

We obtained maximum likelihood estimates (MLEs) of the free model parameters (see Table S2 in the ESI) from the drug uptake profiles obtained with the PS, $\Delta ompF$ and $\Delta tolC$ *E. coli* strains. We compiled a library of 18 datasets by combining population-averaged profiles from: (i) growing PS cells (3 experimental repeats); (ii) growing $\Delta ompF$ cells (3 experimental repeats) and (iii) growing $\Delta tolC$ cells (2 experimental repeats). Under the assumption of Gaussian measurement error, the MLEs for each dataset correspond to parameter values minimising the following sum of squares: $\epsilon = \sum_t \frac{(D_{T,t} - \bar{y}_t)^2}{\sigma_t^2}$. Here, \bar{y}_t is the population-averaged drug uptake measurement at time t ;

$D_{T,t}$ is the drug uptake predicted by the model; σ_t is the measurement error calculated based on a coefficient of variation of 4% (we obtained this from fluorescence measurements of the PDMS background); and the sum runs over all the time-points 0 to 400 s. Minimization was performed using Matlab's in-built nonlinear least-squares solver (lsqcurvefit; using the Levenberg-Marquardt optimization algorithm and with the maximum number of iterations set to 15). To find the global optimum of ϵ , we repeated the minimization task starting from 500 different initial points covering the entire parameter space (generated using a Sobol sequence of quasi-random numbers) and picked the best solution.

We analyzed the single-cell data using a Bayesian hierarchical version of the model in which parameters M_0 and v vary between single-cells. In particular, we postulate that these model-parameters are distributed at the population level according to two independent log-normal distributions (20). Below, M'_0 and v' denote the rescaled versions of M_0 and v which accommodate fitting the model to data normalized by the fluorescence of the drug dose (Table S2). The mean ($\mu_{M'_0}, \mu_{v'}$) and standard deviation parameters ($\sigma_{M'_0}, \sigma_{v'}$) of each log-normal distribution dictate the average value of the corresponding model-parameter and its spread across a bacterial population. Posterior estimates of these population parameters ($\mu_{M'_0}, \mu_{v'}, \sigma_{M'_0}, \sigma_{v'}$) were inferred from single-cell data (biological repeats were treated separately) using Gibbs sampling and informative priors based on the MLE estimates obtained in the step above (see Figures S4, S5 and Table S3 in the ESI). In the first iteration ($j = 1$) of the algorithm $\mu_{M'_0}^{(1)}, \mu_{v'}^{(1)}, \sigma_{M'_0}^{(1)}$, and $\sigma_{v'}^{(1)}$ were drawn from their corresponding prior distributions and for each cell $i = 1, \dots, K$ model-parameters $M'_{0,i}{}^{(1)}, v_i'^{(1)}$ were obtained by minimizing the discrepancy between the model-predicted uptake profile and the single-cell measurements $\mathbf{y}_i = \{y_{i,t} : t = 1, \dots, Z\}$. Subsequent iterations ($j > 1$) involve sampling in-turn from the full conditionals:

- $M'_{0,i}{}^{(j)}, v_i'^{(j)} \sim P(\cdot | \mathbf{y}_i, \mu_{M'_0}^{(j-1)}, \mu_{v'}^{(j-1)}, \sigma_{M'_0}^{(j-1)}, \sigma_{v'}^{(j-1)})$;
- $\mu_{M'_0}^{(j)}, \mu_{v'}^{(j)} \sim P(\cdot | \{M'_{0,i}{}^{(j)}, v_i'^{(j)} : i = 1, \dots, K\}, \sigma_{M'_0}^{(j-1)}, \sigma_{v'}^{(j-1)})$;
- $\sigma_{M'_0}^{(j)}, \sigma_{v'}^{(j)} \sim P(\cdot | \{M'_{0,i}{}^{(j)}, v_i'^{(j)} : i = 1, \dots, K\}, \mu_{M'_0}^{(j)}, \mu_{v'}^{(j)})$.

In our analysis, we used conjugate priors for $\mu_{M'_0}, \mu_{v'}, \sigma_{M'_0}, \sigma_{v'}$, i.e., normal priors for $\mu_{M'_0}$ and $\mu_{v'}$, and gamma priors for $\sigma_{M'_0}^{-1}$ and $\sigma_{v'}^{-1}$. This choice greatly simplifies steps (b) and (c) as the target sampling distributions are the updated normal and gamma distributions, respectively. In step (a) for each cell i we sampled from the target distribution:

$$P(M'_{0,i}, v'_i | y_i, \mu_{M'_0}^{(j-1)}, \mu_{v'}^{(j-1)}, \sigma_{M'_0}^{(j-1)}, \sigma_{v'}^{(j-1)}) \propto P(y_i | M'_{0,i}, v'_i) P(M'_{0,i}, v'_i | \mu_{M'_0}^{(j-1)}, \mu_{v'}^{(j-1)}, \sigma_{M'_0}^{(j-1)}, \sigma_{v'}^{(j-1)})$$

using a single Metropolis-Hasting step with a bivariate normal as the proposal distribution (covariance matrix set to $10^{-4}\mathbf{I}$, where \mathbf{I} is the 2x2 identity matrix). All results presented were obtained by running the Gibbs sampler for 2000 iterations (after having discarded 500 ‘warm-up’ iterations).

Propidium Iodide (PI) staining to test membrane integrity after UV and ofloxacin treatment:

To ensure that the combination of UV (365 nm) exposure and ofloxacin treatment does not compromise the cells’ membranes, we treated PS *E. coli* cells (growing) after an experiment with PI (1 μ l dissolved in 1 ml PBS) for 10 min at a flow rate of 100 μ l/h. PI is a stain commonly used to identify bacterial cells with compromised membranes. PI fluorescence was captured using an mCherry filter set (Chroma) using the green LED for excitation. A combined bright-field and mCherry fluorescence image representative of these experiments is shown in Figure S2, where it can be seen that less than 5% of the cells are stained with PI. Similar levels of PI staining were obtained for cells treated with ofloxacin but not bleached directly with the focused UV light. This suggests that our UV exposures do not compromise membrane integrity for the majority (>95%) of the cells.

References:

1. J. O’Neill. Tackling drug-resistant infections globally: Final report and recommendations. (2016).
2. L. L. Silver. A Gestalt approach to Gram-negative entry. *Bioorganic Med. Chem.* **24**, 6379–6389 (2016).
3. J. Cama, A. M. Henney, M. Winterhalter. Breaching the Barrier: Quantifying Antibiotic Permeability across Gram-Negative Bacterial Membranes. *J. Mol. Biol. in press* (2019). doi:10.1016/j.jmb.2019.03.031
4. J.-M. Pagès, C. E. James, M. Winterhalter. The porin and the permeating antibiotic: a selective diffusion barrier in Gram-negative bacteria. *Nat. Rev. Microbiol.* **6**, 893–903 (2008).
5. D. Du, Z. Wang, N. R. James, J. E. Voss, E. Klimont, T. Ohene-Agyei, H. Venter, W. Chiu, B. F. Luisi. Structure of the AcrAB-TolC multidrug efflux pump. *Nature* **509**, 512–515 (2014).
6. K. Lewis. Platforms for antibiotic discovery. *Nat. Rev. Drug Discov.* **12**, 371–387 (2013).
7. M. E. Falagas, I. A. Bliziotis. Pandrug-resistant Gram-negative bacteria: the dawn of the

post-antibiotic era? *Int. J. Antimicrob. Agents* **29**, 630–636 (2007).

8. X. Liu, T. Ferenci. Regulation of Porin-Mediated Outer Membrane Permeability by Nutrient Limitation in *Escherichia coli*. *J. Bacteriol.* **180**, 3917–3922 (1998).
9. M. Ackermann. A functional perspective on phenotypic heterogeneity in microorganisms. *Nat. Rev. Microbiol.* **13**, 497–508 (2015).
10. D. A. Six, T. Krucker, J. A. Leeds. Advances and challenges in bacterial compound accumulation assays for drug discovery. *Curr. Opin. Chem. Biol.* **44**, 9–15 (2018).
11. J. Vergalli, E. Dumont, J. Pajović, B. Cinquin, L. Maigre, M. Masi, M. Réfrégiers, J.-M. Pagès. Spectrofluorimetric quantification of antibiotic drug concentration in bacterial cells for the characterization of translocation across bacterial membranes. *Nat. Protoc.* **13**, 1348–1361 (2018).
12. L. J. V. Piddock, M. M. Johnson. Accumulation of 10 fluoroquinolones by wild-type or efflux mutant *Streptococcus pneumoniae*. *Antimicrob. Agents Chemother.* **46**, 813–820 (2002).
13. S. Taheri-Araghi, S. Bradde, J. T. Sauls, N. S. Hill, P. A. Levin, J. Paulsson, M. Vergassola, S. Jun. Cell-size Control and Homeostasis in Bacteria. *Curr. Biol.* **25**, 385–391 (2015).
14. D. A. Westfall, G. Krishnamoorthy, D. Wolloscheck, R. Sarkar, H. I. Zgurskaya, V. V. Rybenkov. Bifurcation kinetics of drug uptake by Gram-negative bacteria. *PLoS One* **12**, e0184671 (2017).
15. A. E. Asuquo, L. J. V. Piddock. Accumulation and killing kinetics of fifteen quinolones for *Escherichia coli*, *Staphylococcus aureus* and *Pseudomonas aeruginosa*. *J. Antimicrob. Chemother.* **31**, 865–880 (1993).
16. J. Cama, H. Bajaj, S. Pagliara, T. Maier, Y. Braun, M. Winterhalter, U. F. Keyser. Quantification of Fluoroquinolone Uptake through the Outer Membrane Channel OmpF of *Escherichia coli*. *J. Am. Chem. Soc.* **137**, 13836–13843 (2015).
17. D. C. Hooper. Mechanisms of action of antimicrobials: focus on fluoroquinolones. *Clin. Infect. Dis.* **32**, S9–S15 (2001).
18. J. Cama, M. Schaich, K. Al Nahas, S. Hernández-Ainsa, S. Pagliara, U. F. Keyser. Direct Optofluidic Measurement of the Lipid Permeability of Fluoroquinolones. *Sci. Rep.* **6**, 32824 (2016).
19. M. Schaich, J. Cama, K. Al Nahas, D. Sobota, H. Sleath, K. Jahnke, S. Deshpande, C. Dekker, U. F. Keyser. An Integrated Microfluidic Platform for Quantifying Drug Permeation across Biomimetic Vesicle Membranes. *Mol. Pharm.* *in press* (2019). doi:10.1021/acs.molpharmaceut.9b00086
20. C. Furusawa, T. Suzuki, A. Kashiwagi, T. Yomo, K. Kaneko. Ubiquity of log-normal distributions in intra-cellular reaction dynamics. *Biophysics (Oxf)*. **1**, 25–31 (2005).
21. S. Kaščáková, L. Maigre, J. Chevalier, M. Réfrégiers, J. M. Pagès. Antibiotic transport in resistant bacteria: Synchrotron UV fluorescence microscopy to determine antibiotic accumulation with single cell resolution. *PLoS One* **7**, e38624 (2012).

22. A. Smith, A. Kaczmar, R. A. Bamford, C. Smith, S. Frustaci, A. Kovacs-Simon, P. O'Neill, K. Moore, K. Paszkiewicz, R. W. Titball, S. Pagliara. The culture environment influences both gene regulation and phenotypic heterogeneity in *Escherichia coli*. *Front. Microbiol.* **9**, 1739 (2018).
- 5 23. I. Keren, N. Kaldalu, A. Spoering, Y. Wang, K. Lewis. Persister cells and tolerance to antimicrobials. *FEMS Microbiol. Lett.* **230**, 13–18 (2004).
24. H. I. Zgurskaya, G. Krishnamoorthy, A. Ntrel, S. Lu. Mechanism and function of the outer membrane channel TolC in multidrug resistance and physiology of enterobacteria. *Front. Microbiol.* **2**, 189 (2011).
- 10 25. M. C. Swick, S. K. Morgan-Linnell, K. M. Carlson, L. Zechiedrich. Expression of Multidrug Efflux Pump Genes *acrAB-tolC*, *mdfA*, and *norE* in *Escherichia coli* Clinical Isolates as a Function of Fluoroquinolone and Multidrug Resistance. *Antimicrob. Agents Chemother.* **55**, 921–924 (2011).
- 15 26. R. A. Bamford, A. Smith, J. Metz, G. Glover, R. W. Titball, S. Pagliara. Investigating the physiology of viable but non-culturable bacteria by microfluidics and time-lapse microscopy. *BMC Biol.* **15**, 121 (2017).
27. N. Nikolic, T. Barner, M. Ackermann. Analysis of fluorescent reporters indicates heterogeneity in glucose uptake and utilization in clonal bacterial populations. *BMC Microbiol.* **13**, 258 (2013).
- 20 28. M. R. L. Stone, M. S. Butler, W. Phetsang, M. A. Cooper, M. A. T. Blaskovich. Fluorescent Antibiotics: New Research Tools to Fight Antibiotic Resistance. *Trends Biotechnol.* **36**, 523–536 (2018).
29. P. Wang, L. Robert, J. Pelletier, W. L. Dang, F. Taddei, A. Wright, S. Jun. Robust growth of *Escherichia coli*. *Curr. Biol.* **20**, 1099–1103 (2010).
- 25 30. N. Stuurman, N. Amdodaj, R. Vale. μ Manager: Open Source Software for Light Microscope Imaging. *Microsc. Today* **15**, 42–43 (2007).
31. A. Smith, J. Metz, S. Pagliara. Alpha version of momanalysis.
doi:10.5281/zenodo.1063990
- 30 32. T. Lindeberg. Scale-space theory: A basic tool for analysing structures at different scales. *J. Appl. Stat.* **21**, 225–270 (1994).
33. G. W. Zack, W. E. Rogers, S. A. Latt. Automatic Measurement of Sister Chromatid Exchange Frequency. *J. Histochem. Cytochem.* **25**, 741–753 (1977).
34. S. van der Walt, J. L. Schonberger, J. Nunez-Iglesias, F. Boulogne, J. D. Warner, N. Yager, E. Gouillart, T. Yu, S. Contributors. scikit-image: image processing in Python. *PeerJ* **2**, e453 (2014).
- 35

Funding: J.C. acknowledges funding from a Wellcome Trust Institutional Strategic Support Award (204909/Z/16/Z) to the University of Exeter. J.C. and U.F.K. also acknowledge funding from the BBSRC and ERC (DesignerPores 647144). M.V. and K.T.A. gratefully acknowledge financial support from the EPSRC via grant EP/N014391/1. J.M. is funded by the University of Exeter's Department of Biosciences. A.S. acknowledges funding from the BBSRC via a SWBio-DTP studentship (BB/M009122/1). J.I. acknowledges support from the EU project SINGEK (H2020-MSCA-ITN-2015-675752). S.P. acknowledges funding from an MRC Proximity to Discovery EXCITEME2 grant (MCPC17189), a Royal Society Research Grant (RG180007) and a Wellcome Trust Strategic Seed Corn Fund (WT097835/Z/11/Z).

Author contributions: J.C. and M.V. contributed equally to this work. J.C. and S.P. conceptualized the project. J.C. performed all the experiments, with support from A.S. and J.I. The mathematical modelling and analysis was developed by M.V. and K.T.A. with inputs from J.C. and S.P.; the modelling was implemented by M.V. All the image analysis protocols and modules were developed by J.M. U.F.K. provided experimental resources and guidance. J.C., M.V. and S.P. wrote the manuscript, with input from all the other co-authors.

Competing interests: The authors declare no competing interests.

Supplementary Materials:

Figures S1-S6

Tables S1-S4

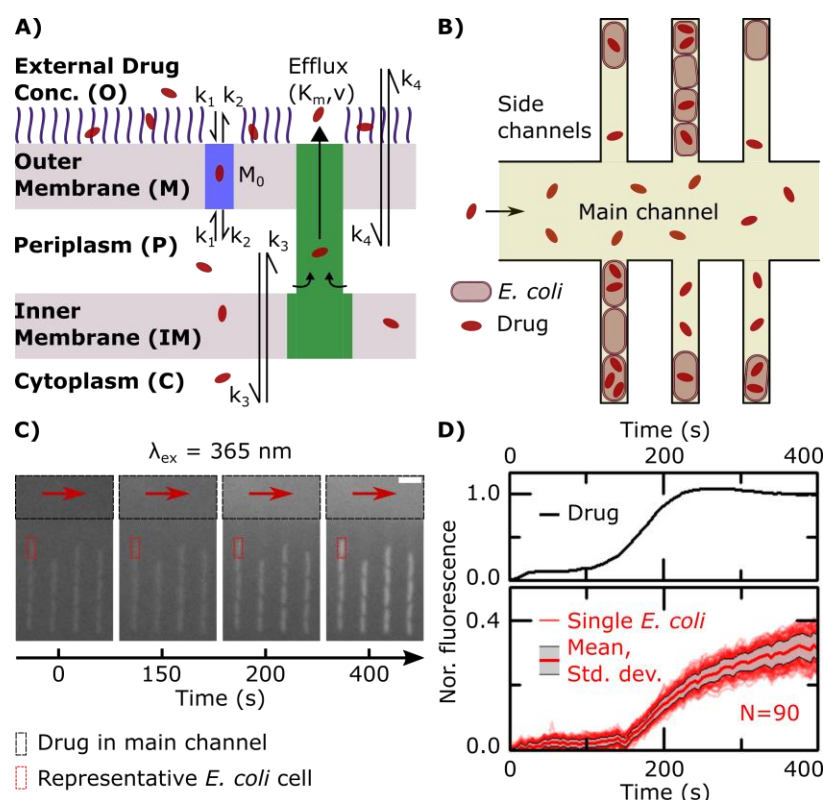


Fig. 1. Quantifying and modelling ofloxacin uptake label-free in individual *E. coli* cells. **A)** Schematic of the main processes involved in drug translocation across Gram-negative cell envelopes. Drug molecules penetrate the outer membrane (M) primarily through protein porins, with association and dissociation rates k_1 and k_2 , respectively. M_0 refers to the concentration of porin binding sites in the outer membrane. Any residual (non-porin) transport across the outer membrane LPS barrier is modelled with k_4 . Drug transport through the inner membrane is modelled with kinetic parameter k_3 . Drug molecules are subject to removal from the cell via active efflux mechanisms which follow Michaelis-Menten kinetics (K_m, v). **B)** Schematic of the microfluidic chip used for the ofloxacin uptake experiment. A main channel of height 25 μm and width 100 μm is used for continuously exchanging the microenvironment with nutrient, drug or dye delivery; cells are confined single-file in a network of side channels whose height and width are both 1.4 μm , with length 25 μm . **C)** Section of epifluorescence images showing the delivery of ofloxacin (100 \times MIC, 12.5 $\mu\text{g/ml}$ in PBS) and its corresponding uptake by the cells in the side channels. The ofloxacin molecules within and around the bacteria are tracked using their auto-fluorescence at $\lambda_{\text{ex}} = 365 \text{ nm}$. Scale bar = 5 μm . **D)** Quantitative estimation of the temporal profile of ofloxacin delivery in the chip, and the corresponding ofloxacin uptake profile of 90 individual *E. coli* cells; the thick red line represents the mean and the grey shaded area the standard deviation of the ofloxacin uptake profiles of the 90 cells investigated. The fluorescence values are reported after correcting for the background and normalizing to the fluorescence of the drug as detailed in the Methods. The complete datasets prior to normalization for the three different *E. coli* strains investigated are presented in the ESI in Figure S6.

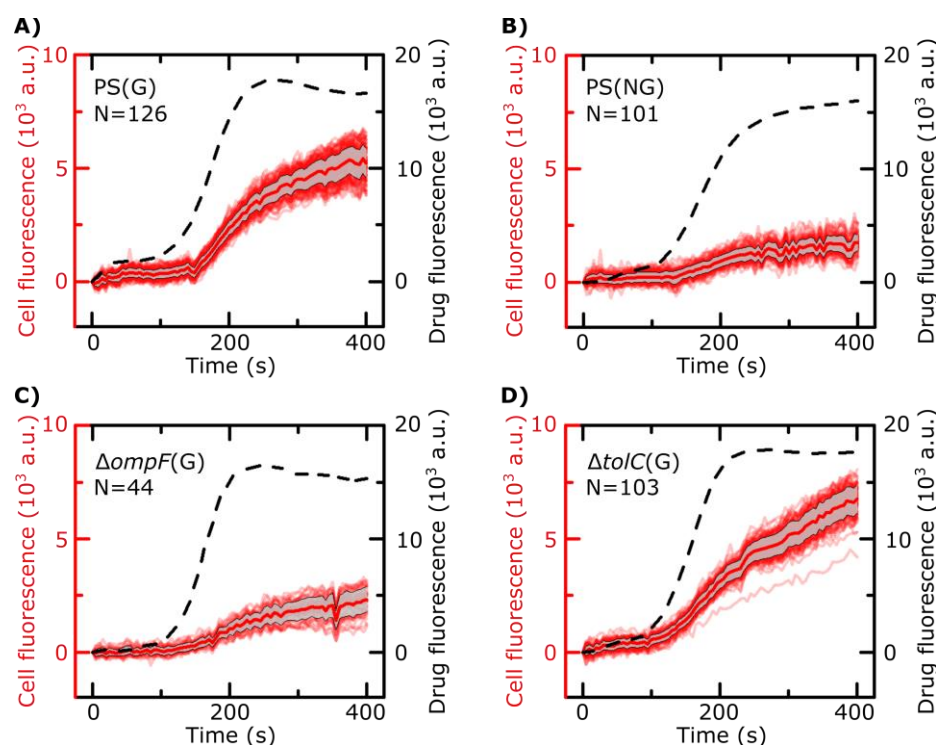


Fig. 2. Representative ofloxacin uptake experiments for the bacterial strains/conditions investigated. The *E. coli* strains (Parental Strain, PS; $\Delta ompF$; $\Delta tolC$), conditions (growing, G; non-growing, NG) and number of cells (N) are indicated inset. All values are reported after subtracting the background and the initial cellular fluorescence (before drug arrival) as explained in the Methods. For reference, the complete datasets for all strains/conditions including all the biological repeats are provided in Figure S6 in the ESI. Dashed lines represent the drug dosage profiles (right Y-axes) in the main channel. These individual drug dosage profiles are provided as inputs when modelling the drug uptake in the corresponding cells in an experiment. The cell fluorescence profiles are shown in red (left Y-axes), along with the mean (thick red line) and standard deviation (grey shading) for all the cells in an experiment. Comparing growing versus non-growing PS bacteria (panels A and B) directly shows that the growing cells accumulate more drug than non-growing cells. This is apparent in the $\Delta tolC$ strain as well (Figure S6). Comparing the cell fluorescence profiles of growing PS (A), $\Delta ompF$ (C) and $\Delta tolC$ (D) also clearly shows that the $\Delta ompF$ mutant accumulates less ofloxacin than the other two strains. A quantitative analysis of the amount of drug accumulated at the end of the experiments for each strain/condition is provided in Figure 3.

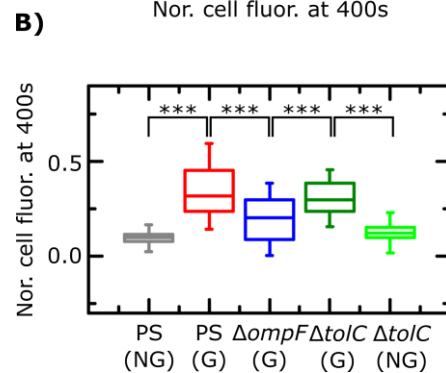
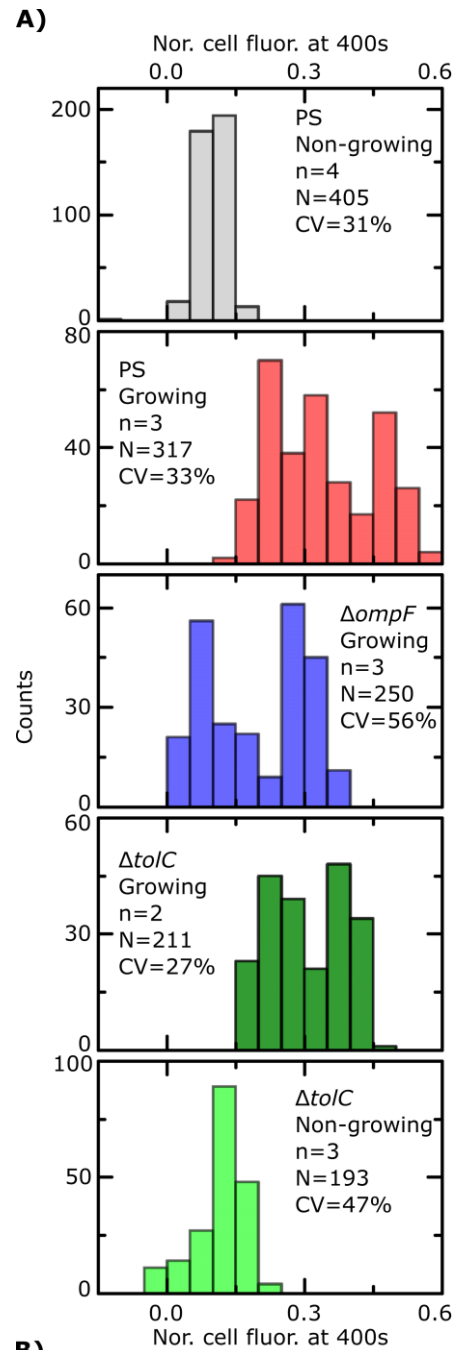


Fig. 3. Final level of normalized whole cell fluorescence for the different strains and nutritional conditions. In the insets, n refers to number of biological repeats, N reports the total number of bacteria and CV refers to the coefficient of variation of the data. All comparisons are made at $t = 400$ s. Comparison of data pooled from the different experiments shows that non-growing PS *E. coli* show significantly lower ofloxacin uptake than growing PS *E. coli* ($p < 10^{-10}$). This was also true in the $\Delta tolC$ strain, where non-growing cells showed significantly lower uptake ($p < 10^{-10}$) than growing cells, suggesting ofloxacin uptake critically depends on the growth phase of the cells within the timescales of our experiment. Growing $\Delta ompF$ *E. coli* showed lower whole cell drug accumulation than growing PS ($p < 10^{-10}$) and $\Delta tolC$ ($p < 10^{-10}$) cells, in line with expectations. Statistical significance tested using a 2-sample t-test incorporating Welch's correction; the complete set of p-values is reported in the ESI (Table S1).

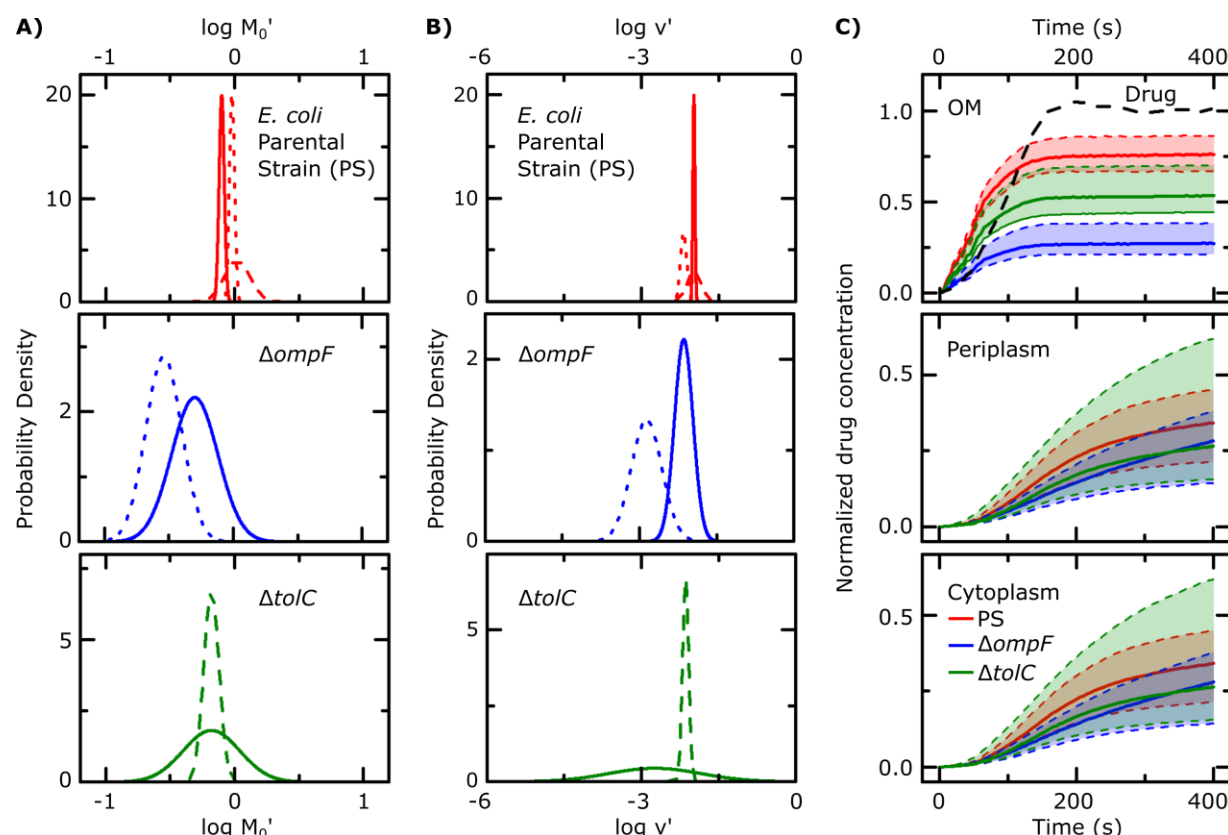


Fig. 4. Drug accumulation kinetics predicted by fitting the single-cell data to the drug uptake model. Maximum a posteriori estimates of parameters M'_0 (A) and v' (B) for growing parental strain (PS, top), $\Delta ompF$ (middle) and $\Delta tolC$ (bottom) *E. coli*. The solid, dashed and dotted lines refer to individual biological repeats. These distributions were generated using the mode of the posterior distributions of the means and standard deviations of the log-normal distributions for M'_0 and v' ; the complete posterior distributions of the means and standard deviations for the parameters are provided in the ESI in Figures S4 and S5 respectively. C) Predicted ofloxacin uptake in the different bacterial compartments. Temporal dependence of the normalized drug concentration in the outer membrane, periplasm and cytoplasm for PS (red), $\Delta ompF$ (blue) and $\Delta tolC$ (green) bacteria in response to the drug dosage input (dashed black line, top panel). These drug uptake profiles were obtained by using the kinetic parameter values in (A) and (B) and the theoretical model (equations (i)-(iii)). The concentrations reported are normalized to the drug dosage concentration (12.5 $\mu\text{g/ml}$ ofloxacin). The solid lines correspond to median accumulation in the respective compartments and the shaded area represents the [20,80] posterior predictive interval of the accumulation. The results shown were generated by running the model using 500 independent samples of parameters M'_0 and v' from the posterior distributions in Figures S4 and S5 respectively. All other parameters were fixed to the values given in Table S2. The model predicts the saturation of binding sites in the outer membrane. The median saturation concentration in the outer membrane is approximately 3-fold higher in the PS compared with the $\Delta ompF$ strain. The periplasmic and cytoplasmic concentrations within each strain are similar as expected from our model, which predicts rapid equilibration between the two compartments based on the passive permeability of ofloxacin across the inner membrane lipid bilayer. Using the [20,80] posterior predictive intervals, we have calculated the probabilities of cells from the different strains showing

higher/lower accumulation in the different compartments in a pairwise manner. These results are provided in Table S4.